

Spectroscopic mapping of the quasar 3C 48 at sub-arcsec resolution*

Eleni T. Chatzichristou¹, Christian Vanderriest², and Walter Jaffe¹

¹ Leiden Observatory, Postbus 9513, 2300 RA Leiden, The Netherlands

² DAEC, Observatoire de Paris-Meudon, 5 place Jules Janssen, F-92195 Meudon Principal Cedex, France

Received 30 July 1998 / Accepted 10 December 1998

Abstract. The quasar 3C 48, an unusual CSS radio source with excess far-IR emission, is known to present morphological evidence for a recent merger. We present here new data on the two-dimensional kinematics and emission line properties of the extended ionized gas, obtained with an integral field spectrograph. We find that the emission lines are split in two components: (i) a fast moving ($\sim 580 \text{ km s}^{-1}$) blue-shifted broad ($\sim 1000 \text{ km s}^{-1}$) component and (ii) a narrow ($\sim 400 \text{ km s}^{-1}$) component at the systemic redshift, spatially resolved at the $0.5''$ level. We detect a faint red continuum knot that is spatially coinciding with the putative second nucleus 3C 48A (Stockton & Ridgway 1991). We discuss the possible origins of the observed alignment between the radio jet $\sim 1''$ NE from the nucleus, the extended ionized emission and the position of 3C 48A.

Key words: galaxies: active – galaxies: interactions – galaxies: kinematics and dynamics – galaxies: quasars: individual: 3C 48 – techniques: spectroscopic

1. Introduction

Two fundamental questions regarding the nature of active galaxies and quasars are (i) the mechanism(s) through which material is fed into the black hole that powers the AGN and (ii) how the energy released in the nucleus is dissipated in the interstellar medium of the host galaxy. Morphological studies of the gas and young stars in the AGN and quasar hosts can provide information on both of these questions. A small number of radio galaxies at low redshift (e.g. 3C 305, 3C 277.3) possess ionized gas halos which show morphologies associated with the radio jets (Miley 1983; McCarthy et al. 1987; Baum & Heckman 1989a, 1989b; Tadhunter et al. 1989; Jackson et al. 1995). This is evidence that the jets interact vigorously with the interstellar gas as they propagate out through the host galaxies. The gas can decollimate and depolarize the synchrotron jets and the radio source can occasionally affect the ionization properties of the

interstellar gas (e.g. Heckman et al. 1981, Heckman et al. 1982; Van Breugel & Dey 1993).

A class of radio sources which may well show extreme interaction between the radio sources and their host galaxies are those characterized by sub-galactic sizes and steep radio spectra that cut-off below 1 GHz. These steep spectrum sources (CSS) are relatively rare, comprising typically $\sim 10\%$ of sources in radio surveys. Here we present observations of an important member of this class, the quasar 3C 48.

3C 48 ($z \sim 0.370$ Greenstein & Matthews 1963) is one of the first quasars to be discovered and for which the host galaxy has been identified (Matthews & Sandage 1963). It is an object of particular interest because of its unusual radio and infrared properties.

3C 48 harbours an unusually steep-core ($\alpha \sim 0.7$) powerful CSS radio source deeply embedded in the host galaxy. Its VLBI radio structure comprises a relatively weak core, elongated N-S and a powerful one-sided jet to the north, highly disrupted at $\sim 0.05''$ from the core through collisions with the dense interstellar medium. This jet then expands out to $\sim 1''$ NE i.e. within the body of the host galaxy (Wilkinson et al. 1991).

3C 48 shows strong far-IR emission, $L = 5 \times 10^{12} L_{\odot}$, (six times larger than in the visual) that dominates its entire luminosity (Neugebauer et al. 1985). This large IR excess cannot be accounted for by simple extrapolation of the radio continuum to far-IR wavelengths. It has been suggested that is due to thermal emission by dust heated by vigorous star formation, induced by the recent merger or/and the interaction of radio plasma with circumnuclear gas confining the jet (Neugebauer et al. 1985; Hes et al. 1995; Stein 1995). The detection of CO emission suggests a large molecular gas mass, $\sim 7 \times 10^{10} M_{\odot}$ (Scoville et al. 1993), but gives no information about its connection to the nuclear activity.

3C 48 is the first quasar for which highly luminous emission line gas was detected (Wampler et al. 1973), the emission extending $\sim 6''$ NW from the nucleus, with a clumpy morphology. North of the nucleus, the line luminosity dominates over the continuum, while the reverse is true $\sim 4''$ to the south. A stellar population of A-type stars was detected in the off-nuclear continuum spectrum (Boroson & Oke 1982, 1984) which could be interpreted either as an aging starburst in the host (probably a large spiral) galaxy or, alternatively, as a young massive stel-

Send offprint requests to: E. Chatzichristou
(chatzich@strw.leidenuniv.nl)

* Based on observations collected with the Canada-France-Hawaii Telescope at Mauna Kea (Hawaii, USA)

lar population forming in a cooling flow (Fabian et al. 1987). The stellar absorption lines have a similar redshift to the broad permitted nuclear lines, indicating that the underlying galaxy is certainly associated with the quasar.

There is important observational evidence suggesting a merger in the recent history of 3C 48: (i) A high surface brightness region $\sim 1''$ NE from the main nucleus was detected in (stellar?) continuum light (with no counterpart in the emission line gas) and was tentatively identified with a second nucleus (Stockton & Ridgway 1991; Hook et al. 1994). (ii) The irregular appearance of the 3C 48 host in optical (presumably stellar) continuum, with a tidal tail-like feature extending $15''$ NW and south of the main body (Stockton & MacKenty 1987; Stockton & Ridgway 1991; Balick & Heckman 1983), that has significantly redder colours than the rest of the galaxy. (iii) The absorption and broad permitted line velocities differ by several hundred km s^{-1} from the narrow forbidden line velocities (Boroson & Oke 1982; Fabian et al. 1987). (iv) IR excess is often associated with merging galaxies.

Very few detailed studies of the jet-gas interaction in radio galaxies exist in recent literature, mostly long-slit spectroscopy (e.g. Clark et al. 1997 and Clark et al. 1998). 3C 48, because of its high AGN luminosity and its relative proximity, seems to be a good candidate to study the processes that drive the kinematics and physical conditions, as well as the morphology, of the line emitting gas. The interpretation of the existing spectral data, in terms of the physical and kinematic structures present, is ambiguous due to poor spatial coverage. To establish the nature of the various gaseous components and to search for kinematic signatures of the radio jet-gas coupling and/or of a recent interaction, we have taken a single 45 min exposure, in sub-arcsec resolution conditions, using an Integral Field Spectrograph (IFS).

2. Observations

The Multi-Object Spectrograph (MOS) was used in the IFS mode (Vanderriest 1995) at the Cassegrain focus of the 3.6 m Canada-France-Hawaii telescope (CFHT). In this configuration, a bundle of 655 optical fibres gives as many simultaneous spectra over a $12'' \times 8''$ field with $0.4''$ spatial sampling. A 45 min exposure was made on the night of October 4th 1996, during a period of excellent seeing ($\sim 0.6''$ FWHM). The spectral resolution (FWHM), measured on night sky lines, is 4.5 \AA and the useful spectral range corresponds to $3000\text{--}5800 \text{ \AA}$ in the rest frame of the quasar. The UV-optical spectra of quasars typically show strong, broad emission lines, the most prominent being the hydrogen Balmer lines and high ionization forbidden lines. Most of these lines are present in the nuclear spectrum of 3C 48, shown in Fig. 7, within the observed spectral region: $[\text{NeV}]_{3426}$, $[\text{OII}]_{3727}$, $[\text{NeIII}]_{3869}$, $[\text{NeIII}]_{3968} + H\epsilon$, $H\delta$, $H\gamma$ + $[\text{OIII}]_{4363}$, $H\beta$, $[\text{OIII}]_{4959,5007}$ and two broad bands of permitted FeII emission line multiplets, near $\lambda 4570$ and $\lambda 5250$ in the quasar rest frame. The raw data are similar to those from a classical image slicer and the basic reduction (flat-fielding, wavelength and flux calibration) is done in an equiv-

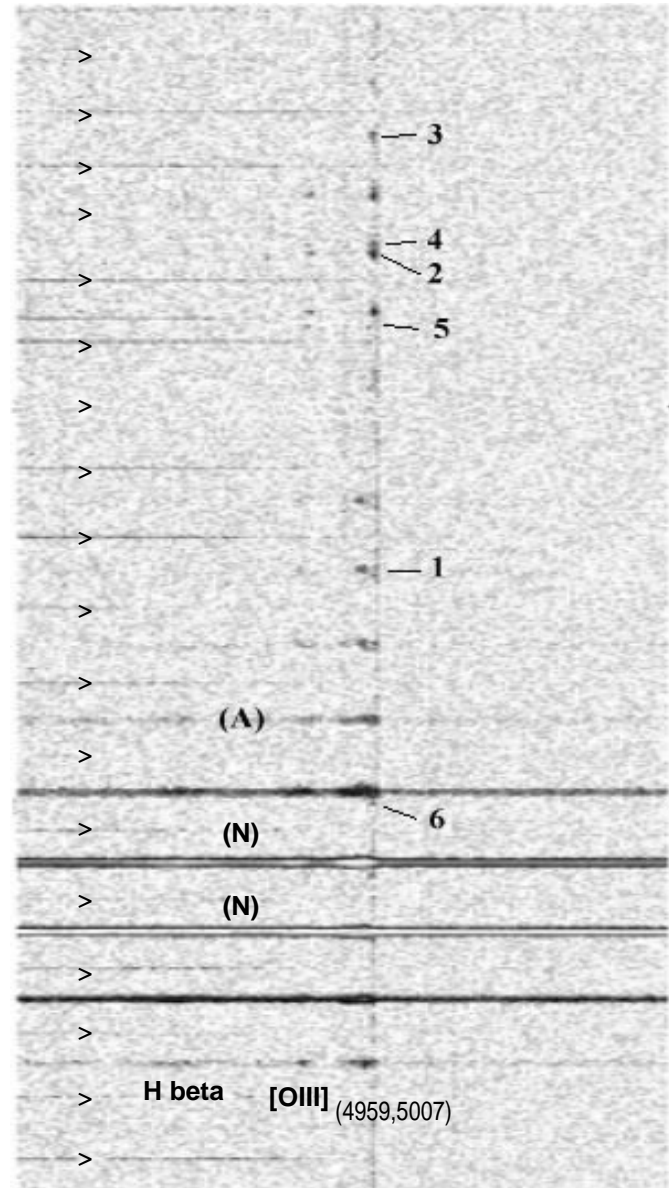


Fig. 1. Portion of the 2D spectroscopic image from MOS/Argus, for the $\sim 5''$ surrounding the 3C 48 nucleus. Each row corresponds to an individual fibre spectrum in the wavelength interval around the $H\beta - [\text{OIII}]_{4959,5007}$ lines (x-direction). The marks on the left side of the figure indicate roughly the starting positions of each row of the hexagonal array, moving from south to north as we go from the bottom to the top of the image. Between two marks, bottom to top indicates east to west direction. The main emission clouds are identified and numbered. The two main rows corresponding to the nuclear region are indicated by (N) and the position of the putative second “nucleus” 3C 48A by (A). The vertical line running through the image next to the $[\text{OIII}]_{5007}$ line is atmospheric OH emission ($\lambda \sim 6863 \text{ \AA}$).

alent way, using standard IRAF procedures; the bidimensional mapping uses a reduction package especially developed for IFS (Teyssandier & Vanderriest 1998).

In Fig. 1 we show a portion of the resulting calibrated “compact” spectroscopic image, where each row corresponds to an

individual fiber spectrum (y -direction) in the $H\beta - [OIII]$ wavelength interval (x -direction). The thick lines indicate strong continuum near the nucleus, while a number of other emission knots are easily seen and numbered for future reference. We characterized the spectrum in each fibre by the following parameters: flux, redshift and dispersion of the various emission lines and the integrated flux in selected portions of the continuum. These are then used to “reconstruct” intensity, velocity and dispersion maps of the observed field. For each spectrum, our reconstruction program first subtracts a mean sky spectrum (constructed from the emission-free fibre spectra) and then fits a *single* gaussian to the selected emission line profile.

In the next section, we discuss in greater detail the spectral characteristics of the individual clouds and the nuclear region of 3C 48.

3. Results

In this section we present the main results from area spectroscopy on the central $(6'')^2$ region of 3C 48. Our data is presented in the form of reconstructed images and 2D maps of various measured quantities, as well as individual (single fibre) and coadded (over regions of interest) spectra. Through this presentation we will be discussing the morphology, the characteristics of the emission line profiles in various wavelengths and, in some greater detail, the kinematics and ionization structure throughout the object.

3.1. Morphology

We have reconstructed a number of intensity/velocity maps, corresponding to several emission lines of interest ($[OIII]_{4959}$, $[OIII]_{5007}$, $H\beta$ and $[OII]_{3727}$). Due to the generally much better S/N of the $[OIII]_{5007}$ line, we will present most of our results using this line, these being consistent with measures on the other detected emission lines unless stated otherwise.

In Fig. 2 we show in grey scale a reconstructed $[OIII]_{5007}$ emission image, with superposed isophotes corresponding to the reconstructed continuum image in the (relatively) line-free spectral range 5110–5840 Å, in the quasar rest frame. This figure shows continuum emission extending $\sim 1.3''$ NE of the apparent nucleus and much more extended line emission to N and NW.

The continuum extension corresponds roughly to the position of “3C 48A”, a high surface brightness region detected by Stockton & Ridgway (1991) in continuum and K-band images. The existence of this potential second nucleus was convincingly shown by Hook et al.(1994) by applying their two channel image restoration technique to the V image of Stockton & Ridgway. In Fig. 1 we indicate with (A) the spectra where the faint redder continuum from 3C 48A is detected. We have deduced synthetic broad band colours, corresponding roughly to the U , B , V standard filters, for the quasar nucleus, 3C 48A and the two strongest emission clouds, **1** and **2**. To do this, we used the integrated spectra (i.e. sum over several fibres) for each region, that were Doppler corrected for the quasar redshift (~ 0.368) and multiplied with the theoretical response curves of the U , B ,

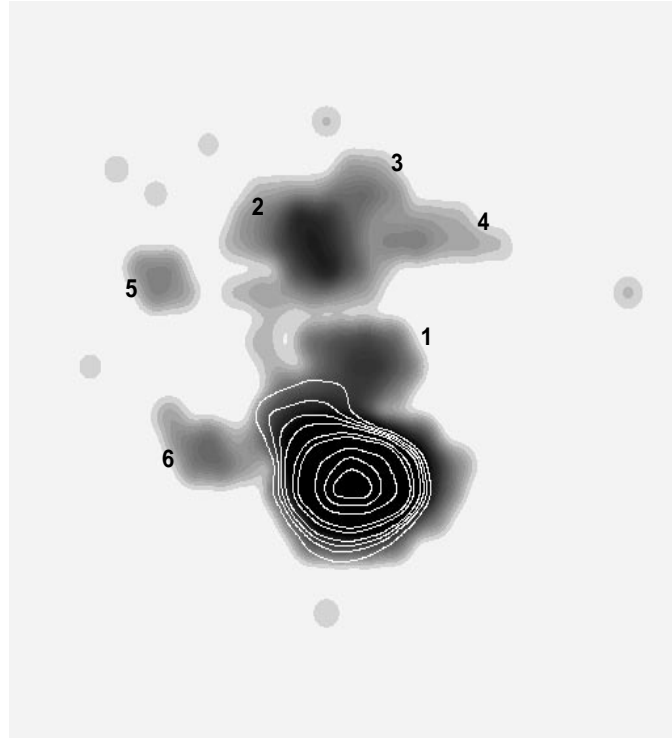


Fig. 2. Reconstructed $[OIII]_{5007}$ intensity image with superposed contours of a reconstructed continuum image, in the central $\sim (6'')^2$ region of 3C 48. The labeled emission clouds correspond to those of Fig. 1.

Table 1. 3C 48: Synthetic colours for different regions of 3C 48

Region	$U - B$ ± 0.18	$B - V$ ± 0.13
Nucleus	-0.73	-0.01
3C 48A	-0.24	0.17
Cloud 1	-0.24	0.06
Cloud 2	-0.55	0.12

V filters in the Johnson system. The continua of the resulting spectra were then fitted with a spline3 function and all emission or absorption features differing by more than 1σ of the fit were removed. Finally, we integrated the flux below the fitted line-free spectra, within the total wavelength range for each band. The resulting magnitudes should be equivalent to broad-band photometry within an aperture of $0.8''$ radius for the nucleus and of $0.6''$ radius for 3C 48A and clouds **1** and **2**. We have repeated this procedure for a few standard stars (including Feige 110 that was used to flux calibrate our spectra). The colours computed this way are listed in Table 1. The uncertainties that are also listed in this table represent mainly the noise errors, the zero-point errors being relatively small. Although the uncertainties in the resulting colours are rather large, of the order of ~ 0.18 mag in $U - B$ and ± 0.13 mag in $B - V$, what is relevant here are the colour differences between the different regions, which do not depend on the zero magnitudes used.

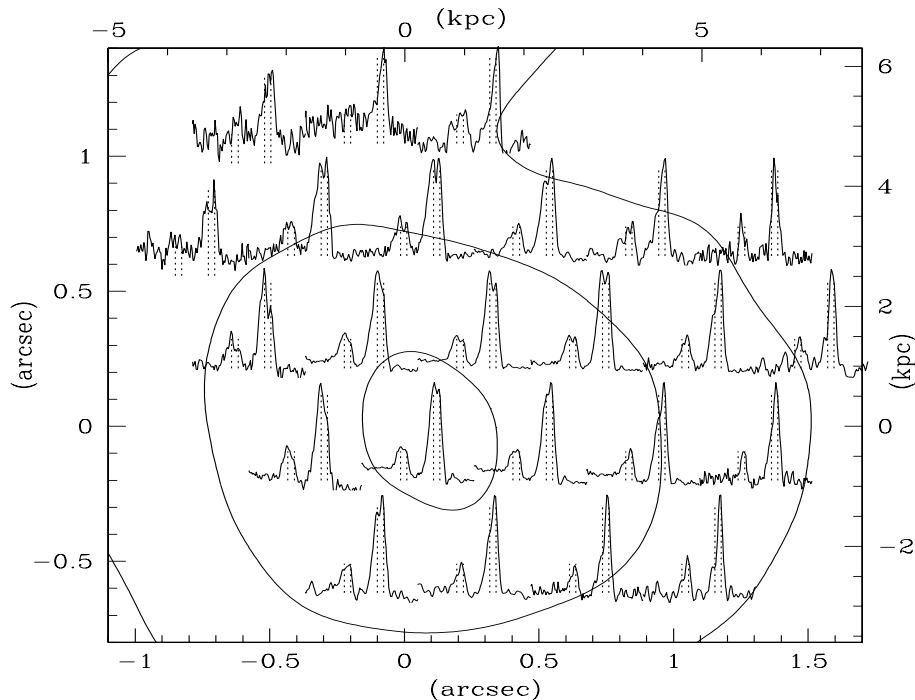


Fig. 3. Spatial distribution of the $[OIII]$ emission line profiles (spectral range 6700–6925 Å), overplotted on the $[OIII]_{5007}$ contour map, within the central $\sim 2'' \times 2.5''$ region of 3C 48. Note the many double peaked profiles. Dashed lines indicate the wavelengths of the fitted components on the integrated nuclear spectrum. For the axes notation in kpc we adopt $z=0.368$, $H_0=75 \text{ km s}^{-1} \text{ Mpc}^{-1}$ and $q_0=0$.

The colours of 3C 48A, although still very blue, are redder than those of the quasar optical nucleus and similar to those of the other emission clouds. This, combined with the observational fact that the emission peak is seen in continuum and K-band light, indicates a redder stellar population rather than higher extinction, in the region of 3C 48A. Indeed there is no evidence for high extinction in this object. Spectroscopic studies infer that $A_V \leq 0.2$ mag, for at least the broad line region (Neugebauer et al. 1979; Fabian et al. 1987). Boroson & Oke (1982, 1984) have detected spectra of an A-type stellar population, in the region of cloud 1. When plotting our results in a typical colour colour diagram for zero-age main sequence stars, we find indeed that the colours of 3C 48A and clouds 1 and 2 correspond roughly to stellar types between A and F. In a more quantitative way, we compare our data with results from the evolutionary synthesis models of Leitherer & Heckman (1995). The colours of 3C 48A and the two emission clouds, if primarily due to a stellar continuum, indicate stars with ages between 6×10^6 – 1×10^7 yr, essentially independently of reddening, for a typical simulation of an instantaneous burst assuming solar metallicity and a Salpeter IMF.

The ionized gas is extended $\sim 5''$ N and NW of the apparent nucleus and a number of individual emission clouds are identified and numbered (the same as in Fig. 1). The cloud 1 (emission peak $\sim 1.6''$ north of the nucleus) shows resolved emission lines and a detectable velocity gradient. The brightest emitting knot is cloud 2 (emission peak $\sim 3.8''$ north), while all the other emission regions are fainter and extended with narrow/unresolved emission lines. The clumpy structure of the extended ionized gas has been noted in previous studies (Stockton & MacKenty 1987; Stockton & Ridgway 1991), but not all the emitting knots have been identified.

3.2. Line profiles and gas kinematics

3.2.1. Nuclear region

In Fig. 3 we plot the $[OIII]_{4959,5007}$ emission line profiles over the $[OIII]_{5007}$ contour map, for the central $2'' \times 2.5''$ region. For clarity, we only show here the spectra with the highest S/N and all profiles are normalized to a peak intensity of 1. The forbidden narrow lines show striking multiple structure, which is a previously unknown feature. At least two components are clearly identifiable in most of the profiles, the barycenter of the lines changing significantly from the nucleus outwards, indicating that the flux ratio of the individual components is also changing throughout this region. To further investigate this we have attempted to deblend the individual profiles for all the emission lines where substructure is obvious and we have measured the corresponding parameters for the individual components.

Various independent methods were applied and inter-compared in order to achieve an accurate profile decomposition. We finally adopted the following procedure:

To fit and subtract the continuum we use the IRAF task CONTINUUM, interactively adjusting the order of the fitting polynomial and the rejection limits in order to achieve a reliable fit. Then, the task NGAUSSFIT is used to actually deblend the emission lines. Here, initial guesses are provided for a set of parameters describing the individual components (assuming multiple gaussian profiles) and some coefficients are initially held fixed. An interactive fit is then made for all the components simultaneously via χ^2 minimization and repeated iteratively until the “best fit” values are obtained for all the parameters free.

Double profiles were clearly detected for the $[OII]_{3727}$ and $[OIII]_{4959,5007}$ emission lines. The $H\beta$ line profiles are very broad everywhere and no independent multi-component fitting

Table 2. Decomposition of the emission lines on the integrated spectrum (sum over 15 fibres) of the nuclear region

Line	δz_b	$(FWHM)_b$ (km s ⁻¹)	$(Flux)_b \times 10^{-15}$ (ergs cm ⁻² s ⁻¹)	δz_r	$(FWHM)_r$ (km s ⁻¹)	$(Flux)_r \times 10^{-15}$ (ergs cm ⁻² s ⁻¹)	ΔV (km s ⁻¹)
[OII] ₃₇₂₇	0	1000±220	9.75±2.4	0.0001	470±70	4.5±2.0	610±150
[NeIII] ₃₈₆₉	0.0001(**)	1010(**)	7.55±0.6	0(**)	380(**)	1.52±0.4	(570)
[NeIII] _{3968+Hε}	0.0001(**)	1010(**)	1.8±0.9	0(**)	380(**)	≤0.9	(570)
[OIII] ₄₉₅₉	0	1020±140	23.0±3.9	-0.0001	370±30	4.18±2.8	570±170
[OIII] ₅₀₀₇	0.0001	1010±130	65.8±9.7	0	380±25	15.1±6.7	570±100
weighted mean	0.3667±(3)	1010±20		0.3694±(5)	400±30		586±15
Single Component							
$H\gamma + [OIII]_{4363}$				0.3695±(4)	2720±260	20.7±2.6	
$(H\beta)_{broad}^{(*)}$				0.3699±(2)	3310±150	68.0±4.4	

Fitted redshifts, full-width-at-half-maxima and fluxes for the blue and red components (denoted by a *b* and *r* suffix, respectively) of each line. For each of the two components we quote the mean redshift and the difference to this mean for each line. The redshift errors given in parenthesis concern the last digit. The errors of the various quantities are estimated as described in the text.

(*) Residual broad component after fitting and subtraction of two narrow components (see text). The flux ratios for the narrow components are given in Table 6.

(**) Redshifts and line widths are fixed to the fitted values for the [OIII]₅₀₀₇ components (see text).

Table 3. Decomposition of the emission lines on the integrated spectrum (sum over 9 fibres) of 3C 48A

Line	δz_b	$(FWHM)_b$ (km s ⁻¹)	$(Flux)_b \times 10^{-15}$ (ergs cm ⁻² s ⁻¹)	δz_r	$(FWHM)_r$ (km s ⁻¹)	$(Flux)_r \times 10^{-15}$ (ergs cm ⁻² s ⁻¹)
[OII] ₃₇₂₇	-0.0001	1330±640	0.57±0.3	0.0005	570±90	0.95±0.2
[OIII] ₄₉₅₉	0.0001(*)	910(*)	0.18±0.1	-0.0004(*)	590(*)	0.37±0.15
[OIII] ₅₀₀₇	0.0001	910±210	0.95±0.3	-0.0004	590±80	1.2±0.3
weighted mean	0.3669±(9)			0.3700±(3)		
Single Component						
[NeIII] ₃₈₆₉				0.3691±(4)	850±190	0.44±0.1

(*) Redshifts and line widths are fixed to the fitted values for the [OIII]₅₀₀₇ components (see text).

could be done accurately. Instead, we have used the fitted components of the [OIII]₅₀₀₇ line profile as templates, to fit simultaneously the $H\beta$ line with two narrow components (some of the $H\beta$ emission must be coming from the NLR) with their fluxes as the only free parameters and a third broad component with all its parameters free. Although the error bars of the fits are significantly larger in this case, the resulting $\frac{[OIII]_{5007}}{H\beta}$ line ratios for each of the narrow components (and for their sum) are reasonable and in agreement (within errors) between the various fibres. The [NeIII]₃₈₆₉ and [NeIII]₃₉₆₈ lines are asymmetric but a two-component fitting was not possible because of the lower S/N. We fit these lines by using again the [OIII]₅₀₀₇ fitted components as templates and let fluxes vary as the only free parameters. In Table 2 we list the results of the profile decomposition for the integrated nuclear spectrum, that is, the sum of the individual spectra of the 15 central fibres corresponding to an area of ~ 1.9 arcsec² (Fig. 7). The velocity split between the two components is 586 ± 15 km s⁻¹, with the red component having similar redshift to the *broad* Balmer emission lines. Boroson &

Oke (1982) found strong stellar absorption lines in the nebulosities 2'' north and south of the nucleus (the first roughly coinciding with our region 1), that show velocities similar to those for the broad permitted nuclear emission lines: $z=0.3700 \pm 0.0002$. This means that the red component in the split nuclear emission line profiles is probably associated with the underlying galaxy and we will call it “systemic”, the other component being thus blueshifted by ~ 580 km s⁻¹ with respect to this.

The error estimates quoted in Table 2 are the root-mean-square errors of the results obtained from the fits of the individual fibre spectra. However for the other regions (Tables 3–5) the S/N of the emission lines is low on most of the individual spectra and the line decomposition was only performed on the integrated spectra. In these cases, error estimates for all parameters are obtained by root-mean-square residual minimization between the fitted gaussians and the data and include both photon statistics and fitting errors. Finally, in the case of unreasonably large errors ($\gtrsim 50\%$ of the value) we quote in Tables 2–5 only the 1σ upper limits of the values.

Table 4. Decomposition of the emission lines on the integrated spectrum (sum over 10 fibres) of the emission cloud **1**

Line	δz_b	$(FWHM)_b$ (km s ⁻¹)	$(Flux)_b \times 10^{-15}$ (ergs cm ⁻² s ⁻¹)	δz_r	$(FWHM)_r$ (km s ⁻¹)	$(Flux)_r \times 10^{-15}$ (ergs cm ⁻² s ⁻¹)
[OII] ₃₇₂₇	0.0005	530±110	0.84±0.2	0.0003	260(**)	0.29±0.06
[NeIII] ₃₈₆₉	0.0007	750±200	0.35±0.1	0.0003	≤500	0.09±0.06
[OIII] ₄₉₅₉	-0.0005	350±70	0.50±0.1	-0.0014	≤530	0.12±0.08
[OIII] ₅₀₀₇	-0.0003	405±30	1.8±0.1	0	260±40	0.38±0.1
weighted mean	0.3678±(3)			0.3705±(2)		
Single component						
$H\beta^{(*)}$			0.3708±(3)	≤250	≤0.11	

(*) At noise limit, uncertain measures.

(**) Line width is fixed to the fitted value for the red component of [OIII]₅₀₀₇ (see text).

Table 5. Decomposition of the emission lines on the integrated spectra of the emission clouds **2–6**

Line	Feature	Cloud 2	Cloud 3	Cloud 4	Cloud 5	Cloud 6
[OII] ₃₇₂₇	δz	0.0003	–	–	–	-0.0003
	$FWHM$ (km s ⁻¹)	unr ^(*)	–	–	–	410±120
	$Flux$ (10 ⁻¹⁵ ergs cm ⁻² s ⁻¹)	0.24±0.1	–	–	–	0.16±0.05
$H\beta$	δz	-0.0001	-0.0006	–	–	0.0001
	$FWHM$ (km s ⁻¹)	unr ^(*)	≤560	–	–	320±140
	$Flux$ (10 ⁻¹⁵ ergs cm ⁻² s ⁻¹)	0.28±0.05	≤0.14	–	–	0.04±0.02
[OIII] ₄₉₅₉	δz	-0.0001	0.0003	-0.0001	0.0001	0.0001
	$FWHM$ (km s ⁻¹)	100±50	230±70	230±100	200±100	290±30
	$Flux$ (10 ⁻¹⁵ ergs cm ⁻² s ⁻¹)	0.08±0.04	0.15±0.03	0.21±0.05	0.17±0.04	0.18±0.02
[OIII] ₅₀₀₇	δz	-0.0001	0	0.0002	0	0.0001
	$FWHM$ (km s ⁻¹)	≤150	unr ^(*)	150±70	≤220	170±15
	$Flux$ (10 ⁻¹³ ergs cm ⁻² s ⁻¹)	2.44±0.05	0.41±0.03	0.47±0.06	0.33±0.03	0.38±0.02
z weighted mean		0.3702±(1)	0.3689±(1)	0.3693±(1)	0.3695±(1)	0.3700±(1)

(*) Unresolved lines i.e. $\text{measured}_{(FWHM)} < \text{instrumental}_{(FWHM)}$.

3.2.2. 3C 48A

We have constructed an integrated spectrum for 3C 48A by summing the spectra of 9 individual fibres in the region of the continuum peak detected on the reconstructed images (Sect. 3.1), corresponding to an area of ~ 1.1 arcsec². The resulting spectrum is plotted on Fig. 7. We see here most of the high ionization emission lines that appear in the nuclear spectrum, but the Balmer lines are absent or, in the case of $H\beta$, very weak and noisy. We also notice the much stronger [OII]₃₇₂₇ emission line relative to the higher ionization [OIII] lines in the 3C 48A spectrum, as compared to the nuclear spectrum. These observations show that the line spectrum of 3C 48A is not seriously instrumentally contaminated by the nuclear spectrum or, alternatively, primarily be due to reflected nuclear light. Additional indication for this is the generally higher redshift (by ~ 0.0002) of the emission lines of 3C 48A, compared to the quasar nucleus. To put upper limits to the nuclear contribution to the emission line spectrum of 3C 48A, we have summed the individual nuclear spectra of

the fibres closest to the 3C 48A location. Assuming that all the $H\beta$ line in the 3C 48A spectrum is nuclear contribution, we scale and subtract the summed spectrum from that of 3C 48A until there is no residual of this line left. In this way, we have estimated a maximum of $\sim 20\%$ and $\sim 60\%$ nuclear contribution to the 3C 48A [OII]₃₇₂₇ and [OIII]₅₀₀₇ line emission, respectively. The line profiles of the stronger lines are double and we have applied the same profile decomposition technique as for the nuclear region; the results are shown in Table 3 for the integrated spectrum of 3C 48A.

3.2.3. Cloud 1

Inspection of various line profile maps (similar to that of Fig. 3) over the whole extent of detected line emission, $\sim (6'')^2$, shows split lines *also* in the region **1** for most emission lines (see also Fig. 7). They are significantly weaker here than on the central region but also much narrower, which allows an easier decomposition of the blend. In Table 4, we list the results for the

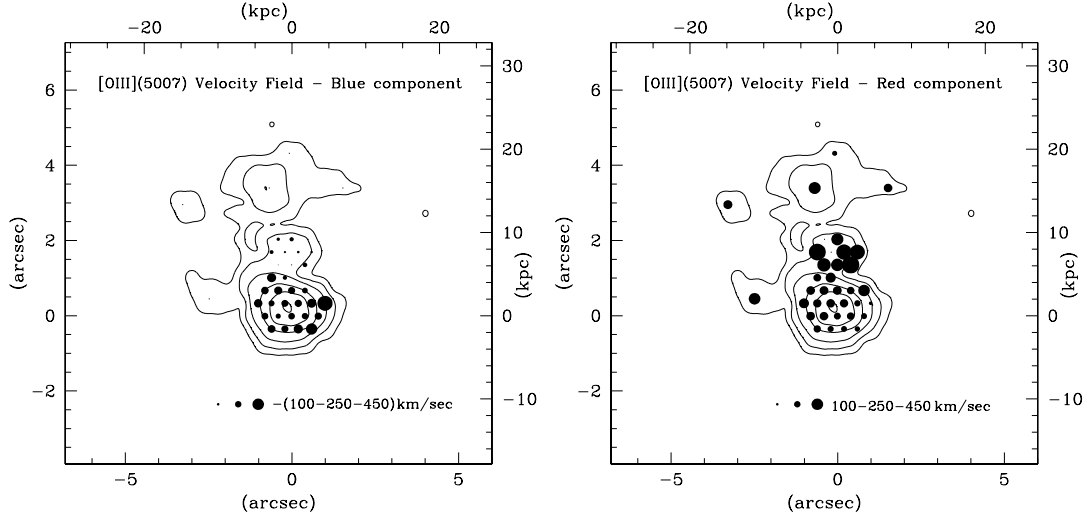


Fig. 4. Distribution of the velocities resulting from the decomposition of the $[OIII]_{5007}$ line. The size of the symbols represents shifts from a reference velocity corresponding to $z=0.368$, that is, larger symbols indicate larger blue-shifts for the blue component and larger red-shifts for the red component. For the axes notation in kpc we adopt $z=0.368$, $H_0=75 \text{ km s}^{-1} \text{ Mpc}^{-1}$ and $q_0=0$.

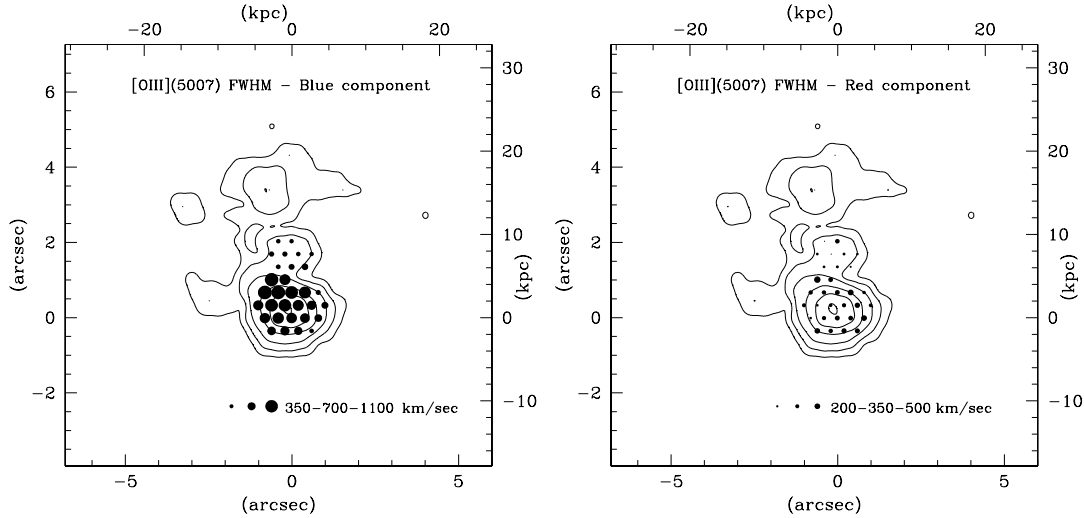


Fig. 5. Distribution of the line widths resulting from the decomposition of the $[OIII]_{5007}$ line. For the axes notation in kpc we adopt $z=0.368$, $H_0=75 \text{ km s}^{-1} \text{ Mpc}^{-1}$ and $q_0=0$.

integrated spectrum of the cloud **1**, summed over 10 fibers (area $\sim 1.3 \text{ arcsec}^2$). Although both components are redshifted (by $\sim 200\text{--}300 \text{ km s}^{-1}$) with respect to those in the nuclear region, the red one shows the same redshift as the broad $H\beta$ line in the same region and similar to the redshift of the absorption lines (0.3713 ± 0.0003) as measured by Boroson & Oke (1982). This agrees with our previous conclusion from the nuclear line profiles, that the red component is most probably associated with the underlying galaxy, while the blue-shifted component represents gas moving in our line-of-sight at speeds up to 580 km s^{-1} .

3.2.4. Analysis of the velocity structure

In Fig. 4 we plot the distribution of velocities resulting from our $[OIII]_{5007}$ profile decomposition superposed on a $[OIII]$

contour map. The size of the symbols represents blue/red-shifts from a reference velocity corresponding to $z=0.368$, arbitrarily chosen, in order to better illustrate the two velocity fields. In the nuclear region, i.e. the central $\sim (2'')^2$, the red/systemic component shows clearly a systematic trend that is probably associated with the rotational velocity field of the host galaxy. The velocity increases from SW to NE with $\Delta V_{max}=200 \pm 35 \text{ km s}^{-1}$. In comparison, there is *no* clear trend in the velocity field of the nuclear blue-shifted component, with a maximum spread of $\Delta V_{max}=260 \pm 145 \text{ km s}^{-1}$. Along the region **1** on the other hand, there seems to exist a gradient in the velocity field of the blue component, with $\Delta V=120 \text{ km s}^{-1}$ within a $\sim 0.8''$ (3 kpc) region. Also, velocities are overall *larger* here (smaller symbols for the blue component and larger for the red) compared to the nuclear region.

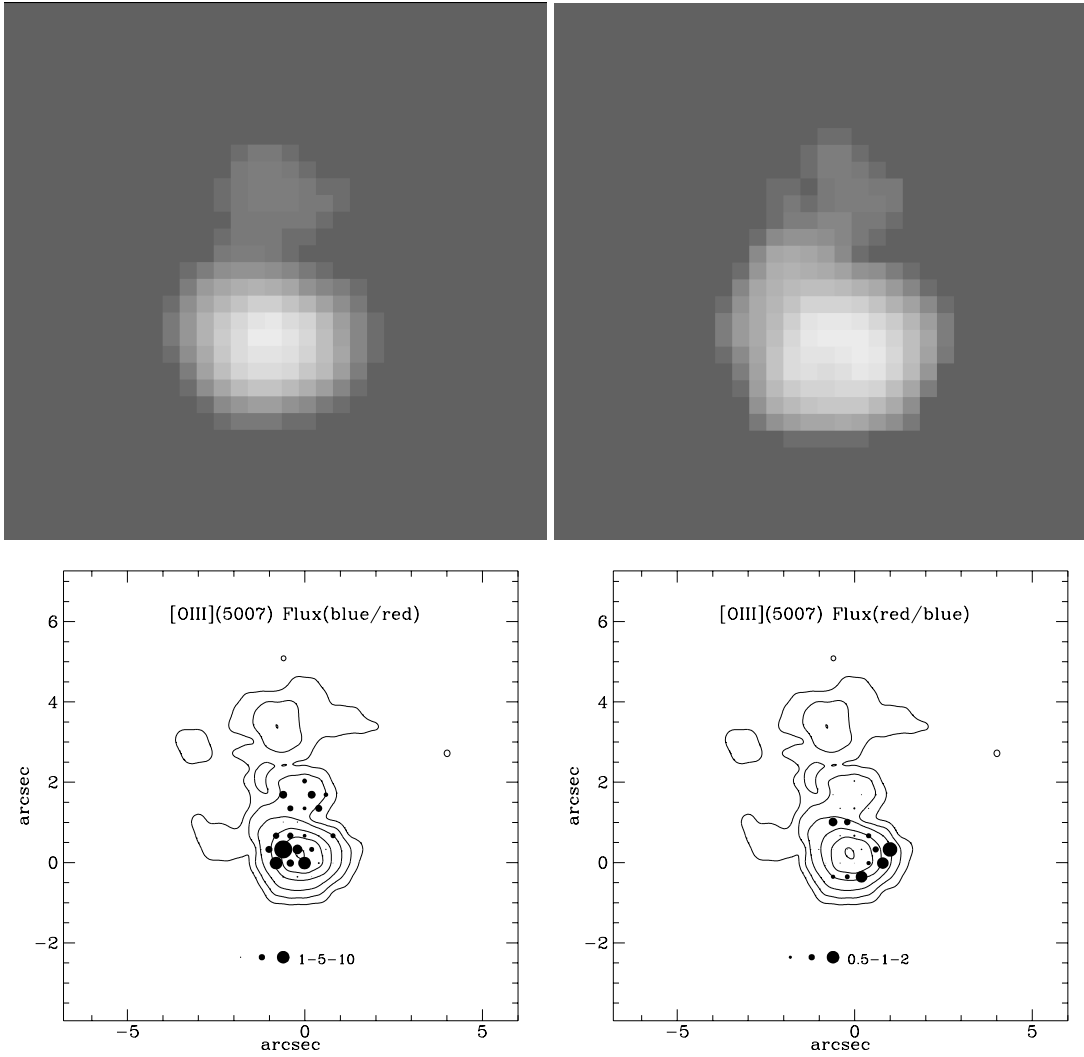


Fig. 6. $[OIII]_{5007}$ blue and red component emission images for the central $\sim(3'')^2$ region of 3C 48, shown on the left and right upper panel, respectively. They are constructed from the results of the profile decomposition in blue and red/systemic components. The lower panels show the spatial distribution of their flux ratios.

The blue nuclear component shows very wide line profiles (up to 1100 km s^{-1}) compared to the much narrower (up to $\sim 510 \text{ km s}^{-1}$) systemic component. This can be seen from Table 2 and Fig. 5 where we plot the line widths (FWHM of the fitted gaussians) for the two components, in a similar way as in Fig. 4. On the left panel we see an obvious trend for the dispersion of the blue component profiles to increase towards the NE i.e. in the same direction as the red/systemic velocity field. There is no systematic trend in the line widths of the red component, except that the narrower profiles occur in the central region. Along the region 1, the narrow emission lines have comparable widths everywhere (with the blue component again somewhat larger than the red), but they remain significantly narrower than the nuclear profiles.

Inspection of Fig. 3, shows also a clear change of the barycenter of the blended line(s) from blue-dominated in the center and eastwards, to red-dominated outwards. We illustrate this effect better on Fig. 6. The upper two panels show

$[OIII]_{5007}$ emission line images for the blue and red components, that we constructed directly from our measures, within the central $\sim(3'')^2$ region (nuclear region and emission cloud 1). In order to see the *relative* importance of the two components, the lower two panels of Fig. 6 show the spatial distribution of the (blue/red) and (red/blue) flux ratios. The four representations are complementary and they essentially show that the blue component is not significantly different from a point source and is dominant in the center and eastwards. The red/systemic component is significantly extended ($\sim 0.6'' = 2.6 \text{ kpc}$) and its barycenter is offset by $0.26''$ (1 kpc) to the west.

All the results that we have presented so far, come directly from measures on the “raw” spectra, the main source of uncertainty being the accuracy of the profile decomposition (which is given by the errors associated with the various quantities). However, when interpreting these results, another important factor to take into account is the limited spatial resolution of our observations. Although the spatial sampling (size of each fiber)

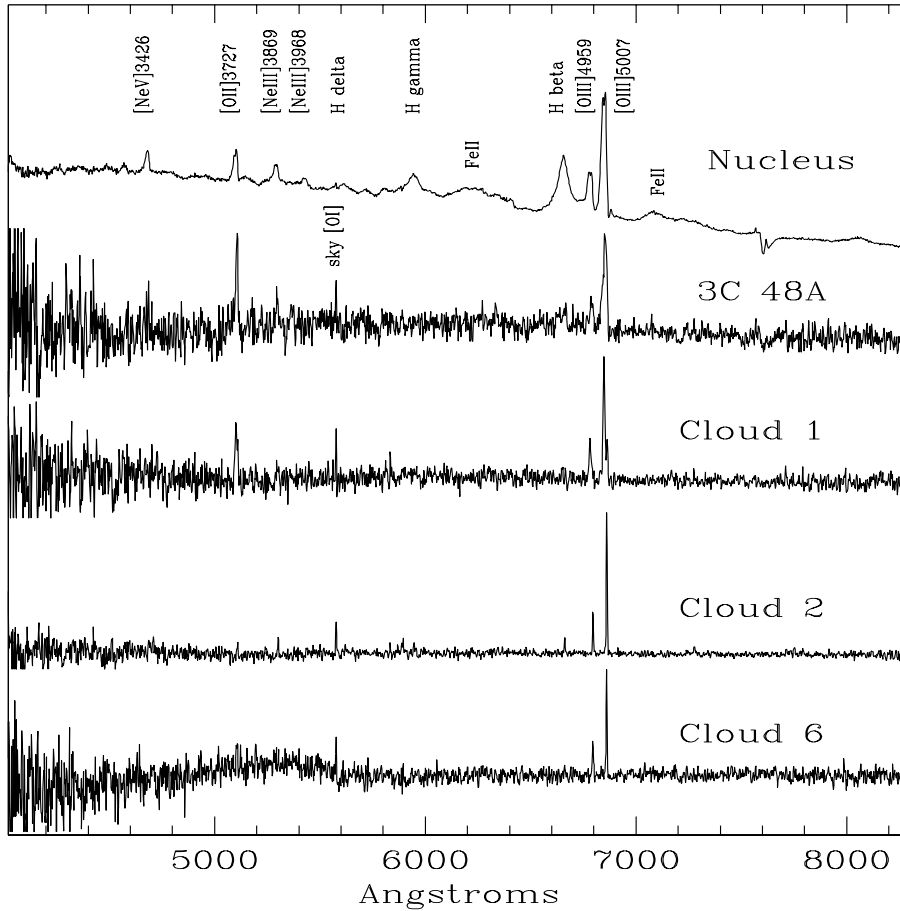


Fig. 7. Normalized, “integrated” spectra (summed over several fibres) for the optical nucleus of 3C 48, 3C 48A and the three brightest emission clouds. The main emission lines (and the residual of the $[OI]_{5577}$ sky line) are identified. Wavelength is in laboratory frame.

is $0.4''$, the seeing during our exposure was $\sim 0.6''$, which is equivalent to a “smoothing” effect between two neighbouring fibres. This does not affect our main results and especially the systematic trends (velocity field and spatial variation of the line widths and barycenters), but it does make it difficult to estimate the *real* (projected) spatial extent of the blue-shifted gaseous component.

Similar plots, as the ones presented above for $[OIII]_{5007}$ were constructed also for the $[OII]_{3727}$ and $[OIII]_{4959}$ lines. They show the same trends but with larger scatter in the measured quantities, due to the lower S/N in these lines. We have also checked the distribution of the $H\beta$ line profiles and associated parameters. Due to the decreasing S/N further from the center, we could not always apply accurately the decomposition in three (two narrow - one broad) components as for the integrated nuclear spectrum. However, our plots show no significant velocity field in the central $\sim (1'')^2$ region, although the line widths show the same trend as the blue narrow-line component, i.e. they are increasing towards the NE (varying between ~ 1800 and 3300 km s^{-1}).

3.2.5. The other emission clouds

In Table 5, we show the results for the most important emission lines measured on the integrated spectra of the remaining five emission clouds, identified on Fig. 1 and 2. The spectrum

of cloud 2 is summed over 10 fibres (area $\sim 1.3 \text{ arcsec}^2$) with peak intensity $\sim 3.8''$ north of the nucleus. This is the brightest emitting knot with the $[OII]_{3727}$, $[NeIII]_{3869,3968}$, $H\beta$ and $[OIII]_{4959,5007}$ emission lines showing symmetric and very narrow (often unresolved) profiles. The measured redshifts for all these lines agree very well (within the errors) with the systemic velocity (i.e. $z \sim 0.37$). The clouds 3 and 4 are further to the NW-W of 2, approximately at $4.8''$ and $4''$ from the nucleus, respectively. They show $[OIII]_{4959,5007}$ emission, with barely any continuum and some $H\beta$ emission, at the detection limit. The line profiles on cloud 4 are asymmetric with a possible faint blue component, but the low S/N does not allow a two-component fitting of the lines. The $[OIII]_{4959,5007}$ emission cloud 5 lies $\sim 4.5''$ NE from the nucleus. In Table 5 we list the measured parameters for the integrated spectra corresponding to these clouds: summed over 5 fibres (area $\sim 0.6 \text{ arcsec}^2$) for cloud 3, over 10 fibres (area $\sim 1.3 \text{ arcsec}^2$) for cloud 4 and over 4 fibres (area $\sim 0.5 \text{ arcsec}^2$) for cloud 5. The mean redshifts are somewhat smaller compared to 2, with a mean z comparable to that of the red/systemic *nuclear* component. Finally, the emission cloud 6 lies at $\sim 2.4''$ east of the nucleus, showing $[OII]_{3727}$, $H\beta$ and $[OIII]_{4959,5007}$ emission lines at a similar redshift to that of cloud 2. The integrated spectrum of 6 (Table 5) is summed over 3 fibres (area $\sim 0.4 \text{ arcsec}^2$).

In Fig. 8 we plot all the integrated spectra in the wavelength range $6400\text{--}700 \text{ \AA}$, normalized to the same peak intensity for

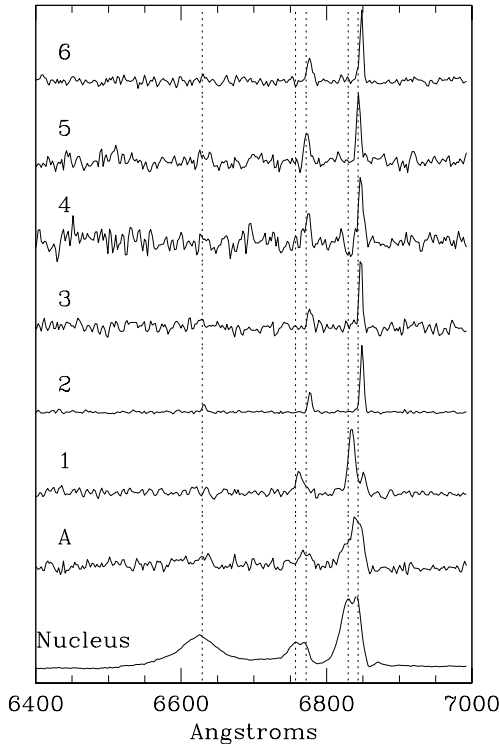


Fig. 8. A portion of the “integrated” spectra near the $H\beta$ and $[OIII]_{4959,5007}$ lines, for the quasar nucleus, 3C 48A and all the identified extended emission clouds of 3C 48, normalized to the same peak intensity. Dashed lines indicate the wavelengths of the fitted nuclear components.

Table 6. 3C 48: Line flux ratios

Region	$\text{Log}\left(\frac{[OIII]_{5007}}{H\beta}\right)$	$\text{Log}\left(\frac{[OII]_{3727}}{[OIII]_{5007}}\right)$
Nucleus (blue)	1.09 ± 0.31	-0.83 ± 0.29
Nucleus (red)	0.70 ± 0.49	-0.53 ± 0.63
Nucleus (total)	0.99 ± 0.24	-0.75 ± 0.26
3C 48A (total)	–	-0.15 ± 0.30
Cloud 1	$(1.46 \pm 0.79)^*$	-0.29 ± 0.21
Cloud 2	0.93 ± 0.17	-1.02 ± 0.46
Cloud 3	0.64 ± 0.56	–
Cloud 6	$(0.97 \pm 3.02)^*$	-0.37 ± 0.29

(*) $H\beta$ at the detection limit

illustration purposes. The dashed lines in Fig. 8 indicate the wavelengths of the two nuclear components in the split $[OIII]$ lines and of the broad/systemic $H\beta$ component. This figure summarizes our main results on the kinematics of the emitting gas in the central $(6'')^2$ region of 3C 48, as presented above.

3.3. Ionization structure

In Table 6, we list the relevant diagnostic emission line ratios for the emitting regions and the two nuclear components (and total, blue+red flux). We have not corrected the line fluxes for reddening, because we cannot estimate the internal extinc-

tion from the present data (the $H\alpha$ line is outside of the observed spectral range and the $H\gamma$ line is blended with the $[OIII]_{4353}$ line). However, previous spectroscopic studies show no evidence for high extinction in at least the broad line region (Neugebauer et al. 1979; Fabian et al. 1987) and unpublished HST images of 3C 48 show no morphological evidence for the existence of dust in the regions of line emitting gas. For the nuclear region, we have computed the line ratios for all the individual fibre spectra, which give similar results with those for the integrated spectrum: the blue component shows everywhere higher ionization than the red/systemic one, the $[OIII]$ emission flux differing by a factor of five between the red and blue (stronger) components, whilst in the $[OII]$ and $H\beta$ lines, the flux ratio is only a factor of two. By summing up the fluxes of the two components we get intermediate line ratios, which are in agreement with results of previous studies (e.g. Stockton & MacKenty 1987). These values are indicative of power-law ionization (Baldwin et al. 1981), which is further strengthened by the presence of strong and broad $FeII$ lines in the nuclear spectrum of 3C 48 (Fig. 7; these lines are characteristic for BLR models associated with the presence of an AGN). In the case of 3C 48A the red component dominates the flux of all emission lines (Table 3) but the blue component again shows higher ionization. In Table 6 we list only the total (blue+red) line ratio, that is subject to smaller error, which clearly shows the presence of lower ionization gas in this region.

It is more difficult to calculate the diagnostic line ratios for the two components on the spectrum of cloud 1, due to the low S/N of the $[OII]$ line and to the weakness, at detection level, of the $H\beta$ line. Consequently, the $\frac{[OIII]_{5007}}{H\beta}$ ratio given in Table 6 is highly uncertain. The relatively large $\frac{[OII]_{3727}}{[OIII]_{5007}}$ ratio reflects again lower ionization for the gas, the $[OII]$ line being an indicator of enhanced star formation. The emission cloud 2 shows an AGN (type 1) - like spectrum, with strong $[OIII]$ and Balmer lines but weaker $[OII]$ lines. For cloud 6 the $\frac{[OIII]_{5007}}{H\beta}$ line ratio is as high as the nuclear value and again we detect additional strong emission from low ionization gas. These detailed results come to support previous suggestions for the existence of a doubly ionized forbidden narrow-line region in this object (e.g. Thuan et al. 1979). These authors have computed an electron density of $\lesssim 10^6 \text{ cm}^{-3}$ for the NLR and of $\gtrsim 10^7 \text{ cm}^{-3}$ for the BLR.

4. Discussion

The main results presented in the previous section are: (i) The detection of double profiles of the high ionization emission lines, over a region of at least $\sim 1''$ around the optical nucleus of 3C 48. These arise from the presence of a gas component blue-shifted by $\sim 586 \pm 15 \text{ km s}^{-1}$ with respect to the systemic component. The narrow emission line widths for the blue component increase to the NE out to $0.8-1''$. This is roughly aligned with the direction of a powerful one-sided radio jet (Sect. 1.1). (ii) The detection of red continuum out to $\sim 1.3''$ NE of the quasar nucleus, possibly coming from a faint secondary nucleus, 3C 48A

(Stockton & Ridgway 1991). This continuum knot roughly coincides with the radio jet/blue-shifted component locations and is somewhat more extended in the same direction.

The spatial coincidence of these three components, if real, is an intriguing result that needs interpretation. There are analogies with cases of other radio sources such as 3C 171, PKS 2250-41 or 3C 305, whose observed properties are mostly explained by the presence of fast shocks driven by the radio jets into the ambient gas (e.g. Jackson et al. 1995, Clark et al. 1997, Clark et al. 1998).

4.1. 3C 48A

We consider three possibilities, in order to explain the extra continuum detected in the location of 3C 48A: (i) scattered light from the active quasar nucleus, (ii) the presence of a second stellar nucleus, merging with 3C 48 and (iii) locally generated continuum, associated with the AGN. (i) Anisotropic emission from the AGN has often been suggested for Seyferts and some radio galaxies. In the case of 3C 48, one could think of nuclear light scattered through the path opened into the ambient interstellar medium, either by the observed $1''$ NE radio jet or, during a previous nuclear/radio activity phase, since the continuum emission seems to be extended somewhat further than the radio structure. We do not know of any polarization studies which could confirm this possibility. However, the optical spectrum of 3C 48A does not seem to be seriously contaminated by nuclear light, as it was shown in the previous section. (ii) The detection of a near-IR counterpart (K' band) to the optical continuum morphology in the region of 3C 48A (Stockton & Ridgway 1991) was interpreted as an indication for the presence of a faint (probably highly obscured) second nucleus. This band corresponds to the H-band wavelength in the quasar rest frame and the above authors give a $V - H$ colour of 2.25 for the galaxy, excluding the (bluer) quasar nucleus and 3C 48A regions. This is roughly the colour expected from a stellar population $6 \times 10^6 - 1 \times 10^7$ yr old, as estimated from our derived optical colours (Sect. 3.1), for a typical simulation of an instantaneous burst assuming solar metallicity and a Salpeter IMF (Leitherer & Heckman 1995). (iii) AGN-associated continuum emission could arise either from synchrotron emission or jet-induced star formation. The first case is less likely because the synchrotron colours, as seen in the nucleus, should be bluer than the observed colours of 3C 48A. Star formation, induced by interaction of the radio jet with the interstellar medium of the host galaxy, seems the most likely explanation for 3C 48A. If intense star formation is what powers the line emission in 3C 48A then, we have shown that the stars must be roughly $6 \times 10^6 - 1 \times 10^7$ yr old. This interpretation is further supported by the diffuse, knotty morphology of 3C 48A as seen on HST images, extracted from the HST archive (Project ID05235, P.I. J.A. Westphal).

Thus, although there is little doubt that 3C 48 has undergone a recent merger, as evidenced by its optical morphology, that has powered the AGN, there is no direct evidence for 3C 48A to be the nucleus of the merging galaxy. Our results provide clues

about its spectroscopic properties, but there is no *direct* way to assess the nature of 3C 48A with the present data. Moreover, our “real” spatial resolution is seeing limited to a little better than 2 fibres. It is clear, that significantly better S/N spectra and seeing conditions that match the instrument spatial resolution ($0.4''$) are required, to improve the detection and measurement of the continuum and of any emission or absorption line spectrum, that could be associated with a “companion” galaxy. Using an IFS system with adaptive optics on a 8m-class telescope seems to be the ideal approach.

4.2. Jet-gas interaction

The radio morphology and optical spectrum of 3C 48 suggest an interaction of its radio jet with its environment. We could have anticipated this, because 3C 48 belongs to the class of Compact Steep Spectrum (CSS) radio sources, whose small sizes could be due to unusually dense environments that confine the radio emission and interact with, possibly disrupting, the radio jet (O’Dea et al. 1991). Numerical simulations have shown that a dense interstellar medium (ISM) may confine CSS sources (De Young 1993), although permanent confinement of the brightest ones would require unrealistic densities and masses. Such sources would rather correspond to a transient state of confinement, by direct collision of the radio jet with very dense ISM condensations. We believe that we see the imprint of such a radio jet - ambient gas interaction in the high velocity blue-shifted narrow emission line component that we have detected throughout the nuclear region of 3C 48. Direct evidence for this is the spatial coincidence of the radio jet with the increasing strength of the blue component, within $0.8 - 1''$ NE from the nucleus. The blue shift of the gaseous material agrees with the view that the one-sidedness of the radio jet is caused by Doppler brightening of material beamed toward us. Conventionally, radio jets from AGNs are assumed to be intrinsically two-sided. The absence of a narrow red-shifted emission line component implies either that 3C 48 is unconventional, i.e. intrinsically one-sided, or that the receding side is not seen. This could be the case if there is no gas intercepting the receding jet, or if that side is obscured by dust.

We have found no systematic velocity field for the blue component, which indicates that it does not participate in the galactic rotation, its projected velocity being predominantly radial. Wilkinson et al. (1991) estimate that the total energy carried by the radio jet on 3C 48 and dumped to the NLR mostly as kinetic energy, would correspond to gas velocities as high as 1000 km s^{-1} . This is comparable to the velocity that we observe for the blue component ($\sim 580 \text{ km s}^{-1}$) relative to the ambient ionized gas emission. Conversely, having an idea of the mass of the line-emitting gas M , of its velocity dispersion σ and of the magnitude of line splitting ΔV , we can estimate the kinetic energy injected to the gas in this region. Fabian et al. 1987 infer the mass of extended ionized gas out to ~ 3 kpc to be $3 \times 10^8 M_{\odot} - 2 \times 10^9 M_{\odot}$ and they estimate the total mass to be 3–6 times larger. Taking $M \sim 10^9 M_{\odot}$, $\Delta V \sim 580 \text{ km s}^{-1}$ and $\sigma = (\text{FWHM})/1.67 \sim 620 \text{ km s}^{-1}$ (taking

the mean FWHM of the blue component), we have $E_{kin} \sim M \times (\Delta V^2 + \sigma^2) \sim 1.43 \times 10^{58}$ ergs. We estimate a dynamical time associated with the outflow in the region of line splitting, $t_{dyn} \sim l/\Delta V$, where $l \sim 1''$ (~ 4.5 kpc, adopting $H_0 = 75 \text{ km s}^{-1} \text{ Mpc}^{-1}$ and $q_0 = 0$). This gives $t_{dyn} \sim 4 \times 10^6$ yr. The rate of energy injection will then be $dE/dt \sim E_{kin}/t_{dyn} \sim 1.13 \times 10^{44} \text{ ergs s}^{-1} = 1.13 \times 10^{37} \text{ W}$. We can compare this to the energy carried by the radio jet, that is likely to be injected to the interstellar medium of the NLR. The radio luminosity of 3C 48 being $\sim 4 \times 10^{37} \text{ W}$, the total amount of energy carried by the jet will be $\gtrsim 10^{38} \text{ W}$ (Wilkinson et al. 1991).

We have shown that the energetics of the radio jet are capable of driving large gas motions in the line emitting regions, similar to the ones that we observe in the nuclear blue-shifted velocity component. A dynamical relationship has indeed long been found between narrow emission line widths and radio power both statistically, in large samples of AGNs (e.g. Heckman et al. 1981), as well as within individual galaxies (e.g. Heckman et al. 1982). Substructure often observed in the emission line profiles of AGNs, coupled to the associated radio components, provides observational evidence for gas outflow in the NLR (Whittle et al. 1988) and model calculations of narrow emission lines that are due to bowshocks driven by radio jets into the ambient gas, seem to support this interpretation (Taylor et al. 1992). Moreover, the high ionization found for the blue-shifted component in 3C 48 and its increasing line widths (up to $\sim 1100 \text{ km s}^{-1}$) in the same direction as the jet expansion (NE), indicate that shock waves could be a source of ionization additional to the AGN ultraviolet flux.

The jet/cloud interaction indicates the presence of a large amount of gas in the region observed (~ 4.5 kpc). Other evidence exists for large amounts of neutral gas in 3C 48, although its total mass, origin and distribution are ambiguous. It has been found, through different kinds of observations, that 3C 48 has large amounts of cold dust and gas: (i) Its large FIR flux indicates a gas mass of $10^{10} M_\odot$. Its far-IR colours suggest that if the radiating dust is heated by the quasar nucleus then it should be concentrated within the central ~ 2 kpc region (Neugebauer et al. 1985). However, it is equally likely that the dust is distributed throughout the disk and is heated by the intense star formation within the host galaxy (Neugebauer et al. 1985; Stein 1995). The present data and recent HST images do not show indications for large amounts of dust in the nuclear few kpc. (ii) CO emission detected in 3C 48 leads to an estimate of a molecular gas mass of $7 \times 10^{10} M_\odot$ (Scoville et al. 1993), with a (deconvolved) size of $1\text{--}1.5''$ ($4.5\text{--}6.8$ kpc, for our adopted cosmology) at a redshift close to the systemic velocity (Wink et al. 1997). The large gas concentration has been claimed to give further support to the merger hypothesis as well as providing with fuel the AGN in 3C 48. Fabian et al. (1987) on the other hand, suggest that 3C 48 is at the center of a massive cooling flow with an inflow rate of $\sim 100 M_\odot \text{ yr}^{-1}$, where some of the inflowing gas maybe fueling the quasar. The same authors find high density ($\sim 50 \text{ cm}^{-3}$) and pressure ($\sim 5 \times 10^5 \text{ cm}^{-3} \text{ K}$) for the ionized gas, that are consistent with the cooling flow interpretation for the gas origin. What-

ever the possible origin(s) for the nuclear gas is, it seems natural to argue that the expanding radio jet will most probably collide with the dense gas clumps of such a rich interstellar medium, warming up material and injecting large amounts of kinetic energy in the emission line region, which is reflected through the blue-shifted velocity component, detected in 3C 48.

We observed the blue shifted second component at ~ 7 kpc ($1.6''$) from the nucleus, in cloud **1**, with a somewhat lower blue-shift: $V_{blue1} - V_{sysNuc} \sim 400 \text{ km s}^{-1}$. This could be material accelerated in shocks near the nucleus, then decelerating as it picks up additional material. The time scale to travel this distance, $\sim 10^7$ yr, is of the same order as the age of the blue stellar population observed here in the continuum (Sect. 3.1); this suggests a common origin.

5. Conclusions

Using a single 45 min exposure on the field of 3C 48 with integral field spectroscopy, we have studied in detail its extended ionized gas properties. Our main results are as follows:

- (i) Multiple emission line profiles indicate the existence of a gas component, which is approaching with a line of sight velocity of $\sim 580 \pm 110 \text{ km s}^{-1}$, with respect to the systemic component. This blue-shifted component is easily detectable on our narrow-line profiles (for the present spectral resolution of 4.5 \AA), while the broad/systemic component dominates the permitted lines. This resolves the issue of the velocity spread between broad and narrow emission lines, reported in previous studies with lower resolution data.
- (ii) The double-peaked narrow emission-line profiles extend $\sim 1''$ around the nucleus, the blue-shifted component dominates the emission in the central region and $\sim 0.6''$ eastwards. Its spatial correlation with the radio jet lead us to argue that this component is the imprint of the jet interaction with the ambient gas. Simple energetic arguments show that the radio jet in 3C 48 is capable of driving the large gas motions that we observe. No corresponding red-shifted velocity component is detected, which is in prima facie agreement with the lack of an observed counter-jet in this object.
- (iii) We detect a red continuum ‘‘knot’’ $\sim 1.3''$ NE from the nucleus, in the same position that Stockton & Ridgway (1991) have discovered a putative second nucleus, 3C 48A. Its spectrum is not significantly contaminated by nuclear scattered light and shows lower ionization gas, probably belonging to the EELR of 3C 48. We argue for a stellar origin for 3C 48A, triggered by the interaction of the radio jet with the dense interstellar medium, its continuum colours indicating a stellar population younger than $\sim 10^7$ yr.
- (iv) The nuclear red/systemic component shows a velocity field, reminiscent of galactic rotation, with $\Delta V_{max} = 180 \pm 35 \text{ km s}^{-1}$, the kinematic axis pointing SE-NW. Other clumps of emission, that we detect mostly north of the nucleus, move with velocities similar to the systemic velocity and are redshifted by $\sim 200\text{--}300 \text{ km s}^{-1}$ with respect to the nuclear (systemic) component. We interpret this velocity difference as an indication that

the gas dynamics in this region might be related to the recent merger.

(v) The nuclear systemic emission component, shows line ratios indicative of photo-ionization by the QSO nucleus. The higher ionization observed for the blue-shifted component indicates an additional ionizing mechanism, this probably being shocks driven by the radio jet into the interstellar medium. The ionization of the strongest emitting clouds (**2** and **6**) shows the existence of an important lower-ionization gas component.

Acknowledgements. We are grateful to G. Miley for very useful discussions and suggestions that helped to improve our understanding and clarify our ideas in the present paper and to P. Best for his critical reading of the manuscript and constructive comments. Thanks are due to A. Lebras and E. Depagne for their help with data processing.

References

- Baldwin J.A., Phillips M.M., Terlevich R.J., 1981, *PASP* 93, 5
 Balick B., Heckman T.M., 1983, *ApJ* 265, L1
 Baum C.W., Heckman T., 1989a, *ApJ* 336, 681
 Baum C.W., Heckman T., 1989b, *ApJ* 336, 702
 Boroson T.A., Oke J.B., 1982, *Nat* 296, 397
 Boroson T.A., Oke J.B., 1984, *ApJ* 281, 535
 Clark N.E., Tadhunter C.N., Morganti R., et al., 1997, *MNRAS* 286, 558
 Clark N.E., Axon D.J., Tadhunter, C.N. Robinson A., O'Brien P., 1998, *ApJ* 494, 546
 De Young D., 1993, *ApJ* 402, 95
 Fabian A.C., Crawford C.S., Johnstone R.M., Thomas P.A., 1987, *MNRAS* 228, 963
 Greenstein J.L., Matthews T.A., 1963, *Nat* 197, 1041
 Heckman T.M., Miley G.K., Van Breugel W.J.M., Butcher H.R., 1981, *ApJ* 247, 403
 Heckman T.M., Miley G.K., Balick B., Van Breugel W.J.M., Butcher H.R., 1982, *ApJ* 262, 529
 Hes R., Barthel P.D., Hoekstra H., 1995, *A&A* 303, 8
 Hook R., Lucy L., Stockton A., Ridgway S., 1994, *ST-ECF Newsletter* 21, 16
 Jackson N., Sparks W.B., Miley G.K., Macchetto F., 1995, *A&A* 296, 339
 Leitherer C., Heckman T.M., 1995, *ApJS* 96, 9
 Matthews T.A., Sandage A., 1963, *ApJ* 138, 30
 McCarthy P.J., Van Breugel W.J.M., Spinrad H., Djorgovski S., 1987, *ApJ* 321, L29
 Miley G.K., 1983, Optical emission from jets. In: Ferreri A., Pacholczyk A.G. (eds.) *Proc. Conf. Astrophysical Jets*. Reidel, Dordrecht, p. 99
 Neugebauer G., Oke J.B., Becklin E., Matthews K., 1979, *ApJ* 230, 79
 Neugebauer G., Soifer B.T., Miley G.K., 1985, *ApJ* 295, L27
 O'Dea C.P., Baum S.A., Stranghellini C., 1991, *ApJ* 380, 66
 Scoville N.Z., Padin S., Sanders D.B., Soifer B.T., Yun M.S., 1993, *ApJ* 415, L75
 Stein W., 1995, *AJ* 110, 1019
 Stockton A., MacKenty J.W., 1987, *ApJ* 316, 584
 Stockton A., Ridgway S.E., 1991, *AJ* 102, 488
 Tadhunter C.N., Fosbury R.A.E., Quinn P.J., 1989, *MNRAS* 240, 225
 Taylor D., Dyson J.E., Axon D.J., 1992, *MNRAS* 255, 351
 Teyssandier P., Vanderriest C., 1998, *ASP Conf. Ser.* in press
 Thuan T.X., Oke J.B., Bergeron J., 1979, *ApJ* 230, 340
 Vanderriest C., 1995, *ASP Conf. Ser.* 71, 209
 Van Breugel W., Dey A., 1993, *ApJ* 414, 563
 Wampler E.J., Baldwin J.A., Burke W.L., Robinson L.B., 1973, *Nat* 246, 204
 Whittle M., Pedlar A., Meurs E.J.A., et al., 1988, *ApJ* 326, 125
 Wilkinson P.N., Tzioumis A.K., Benson J.M., et al., 1991, *Nat* 352, 313
 Wink J., Gilloteau S., Wilson T., 1997, *A&A* 322, 427